First-Principles Investigation of MoS$_2$-MXene Heterostructures as Cathodes in Magnesium Ion Batteries

IISER PUNE

A thesis submitted towards partial fulfilment of

BS-MS Dual Degree Programme

by

ASEEM RAJAN KSHIRSAGAR

20121105

INDIAN INSTITUTE OF SCIENCE EDUCATION AND RESEARCH PUNE

under the guidance of

PROF. UMESH V. WAGHMARE

JAWAHARLAL NEHRU CENTRE FOR ADVANCED SCIENTIFIC RESEARCH, BENGALURU

Certificate

This is to certify that this dissertation entitled 'First-Principles Investigation of MoS_2-MXene Heterostructures as Cathodes in Magnesium Ion Batteries' submitted towards the partial fulfilment of the BS-MS dual degree programme at the **Indian Institute of Science Education and Research, Pune** represents work carried out by Aseem Rajan Kshirsagar at **Jawaharlal Nehru Centre for Advanced Scientific Research, Bengaluru**, under the supervision of **Prof. Umesh V. Waghmare** (Theoretical Sciences Unit) during the academic year 2016-2017.

Student

Aseem Rajan Kshirsagar

Supervisor

Prof. Umesh V. Waghmare

Declaration

I hereby declare that the matter embodied in the report entitled 'First-Principles Investigation of MoS_2-MXene Heterostructures as Cathodes in Magnesium Ion Batteries' are the results of the investigations carried out by me at the **Theoretical Sciences Unit, Jawaharlal Nehru Centre for Advanced Scientific Research, Bengaluru**, under the supervision of **Prof. Umesh V. Waghmare** and the same has not been submitted elsewhere for any other degree.

Student

Aseem Rajan Kshirsagar

Supervisor

Prof. Umesh V. Waghmare

Acknowledgements

Abstract

Technological advancements in the field of energy storage are crucial for an efficient and large-scale use of the renewable energy sources. With the Lithium-ion batteries reaching their maximum theoretical limits of capacity, multivalent ion batteries have attracted attention. High charge storage capacity of the Magnesium anode, multivalency of the Magnesium ion, the high reduction potential, and the large abundance of Magnesium in Earth's crust (2.1 %) are the main advantages of Magnesium-Ion Batteries (MgIBs). Sluggish diffusion of Magnesium atoms into intercalation cathodes and low working voltages offered by cathodes are two of the important challenges in improving the performance of MgIBs. In this work, we propose to use the heterostructures of two-dimensional materials as cathodes in MgIBs. Layered two-dimensional materials have a distinct advantage over the other materials as they can provide enormous area for adsorption and the large interlayer spacings can permit the diffusion of atoms. We have studied, using first-principles density functional theory calculations, the application of two-dimensional heterostructure of MoS_2 and Ti_2CO_2 as possible cathode materials in MgIBs. Motivation for integration of MoS_2 and Ti_2CO_2 is to exploit their individual properties crucial for improving the MgIB cathodes. Previous studies reveal that MoS_2 can allow fast diffusion of Mg atoms on its surface whereas, Ti_2CO_2 can offer large gravimetric capacity. We thoroughly studied energetics of Mg adsorption on MoS_2 and Ti_2CO_2, and also compared their diffusivity using phenomenological models. We have estimated that high intercalation energy (3.52 eV for 11% and 2.63 eV for 100% intercalation sites occupied) and slowly varying discharge curve can be obtained using MoS_2-Ti_2CO_2 as MgIB cathode. Further, interlayer distance tuning of the heterostructure can facilitate much faster diffusion (energy barrier less than 0.1 eV) of Mg through interlayer spacing. Experimental studies are required to gain further insights to improve the design of cathode. We have also pointed out the discrepancy between the theoretical estimate of the voltage of MgIB with MoS_2 cathode and Mg bulk anode and observed voltage for the same battery system, which needs to be addressed.

Contents

List of Tables

List of Figures

Chapter 1

Introduction

From smartphones to automobiles, batteries are an essential part of most of the portable devices. Technological advancements in batteries are becoming more and more important with increased use of renewable energy sources. One of the obstacles in large scale usage of renewable energy sources is variations in their availibility over seasonal cycles, day-night cycles, weather changes, etc. Hence, large-scale, inexpensive and efficient storage of renewable energy is a primary requirement for reducing dependence on fossil fuels which have created many environmental problems. On the other hands, the rapid development of portable devices such as laptops, smartphones, GPS, etc. have increased the power requirements of these devices. This increase power requirement has also contributed to the increased demand of the batteries.

High energy density and power density are the desirable properties of batteries. For a car which runs on battery power, the increase in energy density would allow the car to run for longer distances and the increase in power density would allow the car to have higher acceleration and speed. With Lithium ion batteries reaching their capacity limits, multivalent ion batteries such as Magnesium, Zinc and Aluminium ion based batteries have attracted the scientific community and battery manufacturing giants.

$$\text{Energy Density} = \frac{\text{Charge tranferred during discharge(Q)} \times \text{Voltage(V)}}{\text{Weight of battery}} \tag{1.1}$$

During the process of discharge of a battery, cations move towards cathode and deposit on (or intercalate into) the cathode. To achieve higher energy density, we need lighter cathode materials which can accommodate high quantity of cations. Layered materials
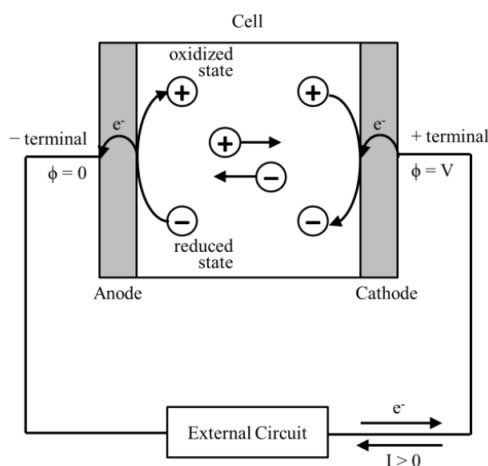
Figure 1.1: Galvanic working of electrochemical cell [1]

can accommodate molecules or atoms between the layers and are suitable candidates as cathode materials.

Magnesium ion batteries (MgIBs) can reach higher energy density because of two reasons: (A) Mg can lose two electrons to form Mg^{2+}, this doubles the charge transfer per cation compared to monovalent cations such as Li^+; (B) its high reduction potential (2.38 V w.r.t. standard hydrogen electrode [3]). Higher reduction potential can generate a larger voltage for MgIBs. Mg anode has very high gravimetric capacity of 3833 mAh/g (Li anode: 2046 mAh/g). Widely used Li ion batteries suffer from formation of dendrite-like structure of Li atoms over many recharge cycles. This can short-circuit Li-ion batteries leading to failure of battery as well as explosions. Electrochemical deposition of Mg on electrodes has been found to be free of such dendrite formation, reducing the concerns regarding safety and durability of MgIBs [4]. Another practical advantage of MgIBs is the large abundance of Mg in Earth's crust (2.1%; around 1000 times the abundance of Li). An important milestone in devising MgIB was the prototype developed by Aurbach et. al. in 2000 [5] which demonstraed a working MgIB. There are two main roadblocks in improving MgIB's performance: (1) disintegration of electrolytes due to reduction by Mg, (2) sluggish diffusion of Mg into intercalation cathodes. Detailed discussion on challenges in improving MgIBs can be found in reference [6].

In this work, we have attempted to design a layered intercalation cathode material by integrating two different 2-dimesnsional materials, MoS_2 and Ti_2CO_2 (MXene), in the form of a heterostructure which can produce higher voltage and also sustain high current density. In layered and 2-dimensional cathode materials, current density de-

7

pends on the energy barriers associated with diffusion of adsorbed/intercalated Mg on surface/interlayer spacing of such materials, and the voltage of a battery depends on free energy change associated with adsorption or intercalation of the carrier cation.

1.1 Two Dimensional Materials as Cathodes in Batteries

The energy density of battery directly depends on charge storage capacity of electrode materials. Layered 2D materials have very large surface area, where ions/atoms can bind, compared to 3D bulk materials; therefore, they can have enormous charge storage capacity. High capacity Graphite anodes are widely used in commercial Li ion batteries. We selected MoS_2 and Ti_2CO_2 for our study for the reasons discussed below.

MoS_2

MoS_2 is probably the second most studied 2-dimensional material after Graphene. It has found applications as a lubricant for a long time and has shown promising properties to be a building block of many electronic, energy conversion and other novel devices [7, 8, 9]. MoS_2 is also found to perform well as a cathode in MgIB experimentally [10]. Highly reversible electrochemical performance was observed with 95 % retention of capacity of 170 mAh/g after 50 charge-discharge cycles. Recent theoretical study shows that energy barriers associated with Mg diffusion on MoS_2 is as low as 0.2 eV. Low energy barriers associated with diffusion are crucial in improving the rate performance of batteries.

Ti_2CO_2

Ti_2CO_2 is a surface terminated form of Ti_2C MXene. MXenes are recently discovered [11] family of 2D materials with general formula: $M_{N+1}X_NT_x$ (M: Transition Metal; X: C or N; T: O, F or OH). MXenes are synthesized by selective itching of $M_{N+1}AX_N$ phases using HF (A belongs to group 13 or 14) [2]. $M_{N+1}AX_N$ phases are a large family of layered solids with more than 70 members. DFT calculations have played a crucial role in predicting structures of MXenes, predicting possible new MXenes, screening their properties and designing devices using them. Many MXenes such as Ti_2C, V_2C, Mo_2C, Ti_3C_2, etc. have been prepared and efforts are being taken by many research groups to reveal more

about the physics and chemistry of MXenes [12]. Experimentally synthesized MXenes are always covered with different terminations such as F, O or OH. These terminations interact with X to satisfy its dangling bonds. Ti_2CO_2 has been studied previously as an electrode in Li-ion battery [13]. A decent gravimetric capacity of 225 mAh/g for a C/25 rate (battery fully discharges in 25 hours) was obtained in the experiment. In an another experimental study, spontaneous intercalation of Mg cations into $Ti_3C_2T_x$ was observed, and a high specific capacitance (100 F/g) was achieved for the Mg intercalated into the MXene [14].
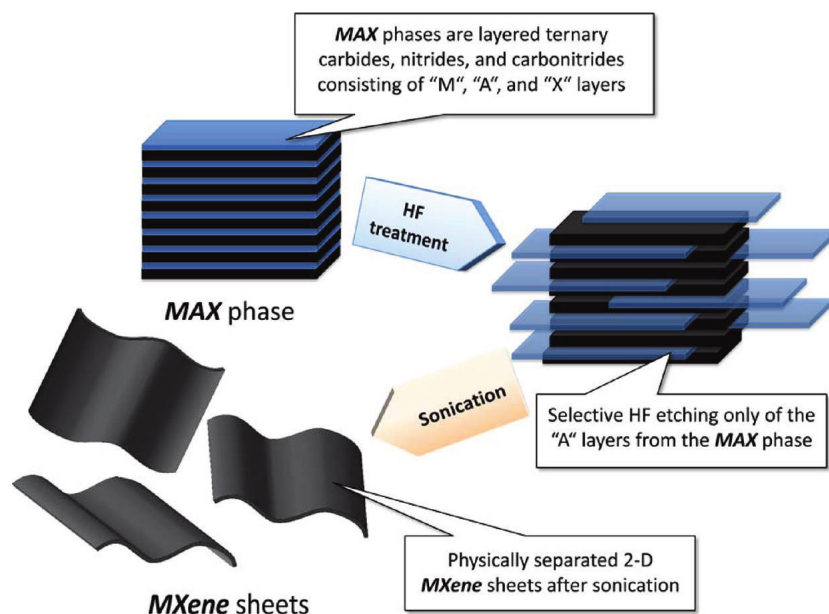
Figure 1.2: Schematic of synthesis of MXenes (Reproduced with permission. Copyright: American Chemical Society, 2012) [2]

Ti_2CO_2 MXene has already been studied using first principles methods for its structural, electronic and vibrational properties [15, 16]. Being one of the lightest MXenes, Ti_2CO_2 can achieve higher gravimetric charge storage capacity. In a computational study by Xie, et.al., the energy barrier associated with diffusion of Mg on surface of Ti_2CO_2 was estimated to be around 0.7 eV. The same study determined the charge storage capacity of Ti_2CO_2 monolayer for Mg as charge carrier to be 570 mAh/g (around 2.5 times that of MoS_2 [10]). We calculated the energy of adsorption of Mg on Ti_2CO_2 to be as high as 2.687 eV (more than 6 times as in the case of MoS_2).

Considering and comparing how Ti_2CO_2 and MoS_2 interact with Mg, we realized that MoS_2 offers faster diffusion of Mg and Ti_2CO_2 can offer a larger storage of Mg atoms and higher binding energy (binding energy $\propto$ voltage). Both features are essential for an

improved MgIB. A general rule in layered 2D materials is that a higher binding energy for an intercalant is also linked with a higher energy barrier for diffusion. Combination of different materials can be a possible strategy of achieving higher binding energy for Mg adatoms/intercalant and lower energy barriers associated with diffusion. To explore this idea, we have studied heterostructures of Ti_2CO_2 and MoS_2 as possible MgIB cathodes.

Exfoliation of layered materials is one of the techniques for increasing access to the adsorption/intercalation sites which cannot be accessed due to sluggish diffusion. Exfoliation impacts the volumetric charge storage capacity negatively due to increase in volume. Alternatively, tuning of interlayer distance by insertion of electrochemically inert polymer (Polyethylene Oxide) has been suggested as a strategy to speed up diffusion by reducing hindrance. It is expected that tuning interlayer distance of layered electrodes will not affect the volumetric charge storage capacity as much as the reduction in particle size or exfoliation can. This method has been tested experimentally for MoS_2 and significant improvement in diffusivity (100 times) has been documented [17]. A theoretical study of the effect of tuning of interlayer distance on intercalation of Mg into MoS_2 has also demonstrated reduction of the energy barriers associated with diffusion through interlayer spacing (80% decrease) and also some decrease in intercalation energy (23% decrease) [18]. The strategy of tuning interlayer distance can be much more beneficial in case of Ti_2CO_2-MoS_2 heterostructure. Faster diffusion can be facilitated using surface of MoS_2 and high intercalation energy can be achieved using surface of Ti_2CO_2. This thesis presents a computational study of Ti_2CO_2-MoS_2 heterostructure as MgIB cathode and discussion about possible ways of engineering the proposed cathode to achieve better performance.

1.2   First-Principles Approach To Battery Materials

Accuracy and computational efficiency of density functional theory (DFT) calculations make them one of the most widely used first principles methodology for study of materials. DFT calculations have been used to determine energetics of intercalation/adsorption and structural changes occurring during charge-discharge processes of cathodes for MgIBs as well as LIBs [19, 20]. There can be considerable discrepancies in theoretical estimates and experimental results due to many reasons including the intrinsic errors associated

with DFT calculations, different physical conditions in experimental setups, defects in experimentally synthesized materials and presence of other chemical entities in experiments. Despite these limitations and inability to handle systems with very large number of atoms due to huge computational complexity, DFT calculations can guide (and misguide if not used carefully) in design of new electrode materials. Screenings of material properties and strength of their interactions with different cations have been done for different families of materials such as MXenes [21].

Using DFT calculations, we have estimated properties of Ti_2CO_2-MoS_2 heterostructure relevant to its performance as MgIB cathode. We have calculated energy changes associated with intercalation of Mg into the heterostructure. We have also explored the strategy of tuning interlayer distance to facilitate diffusion of Mg atoms by estimating energy profile of diffusion. We find that Ti_2CO_2-MoS_2 heterostructure is a promising MgIB cathode and should be synthesized and tested experimentally to gain more insights.

Chapter 2

Theoretical Framework and Methods

Last few decades have witnessed numerous developments in theoretical condensed matter physics, many body theory, and computer technology. Owing to these developments, the field of computational material science has flourished and contributed to better understanding and design of materials. Accuracy, wide applicability and transferability are the key features making Density Functional Theory (DFT) one of the most widely used theoretical tools for studying physics of materials. This chapter concerns the underlying theory of computational methods used for the project, namely, DFT and ways of its implementation using computers.

2.1   Interacting Nuclei and Electrons

Any material made up of atoms can be described by the interactions among the nuclei and electrons which make up the atoms. The general Hamiltonian for such interactions can be written as follows:

$$\hat{H}_{total} = -\frac{\hbar^2}{2m_e} \sum_i \nabla_i^2 - \frac{\hbar^2}{2M_I} \sum_i \nabla_I^2 + \frac{1}{2} \sum_{i \neq j} \frac{e^2}{|r_i - r_j|}$$
$$+ \frac{1}{2} \sum_{I \neq J} \frac{Z_I Z_J e^2}{|R_I - R_J|} + \sum_{i,I} \frac{Z_I e^2}{|r_i - R_I|} \tag{2.1}$$

where, lowercase subscripts correspond to electrons and uppercase subscripts correspond to nuclei, r_i : position of ith electron, R_I : position of Ith nucleus, Z_I : charge on Ith nucleus, m_i : mass of electron M_I : mass of Ith nucleus. The terms in above equation correspond to (1) kinetic energy of electrons, (2) kinetic energy of nuclei, (3) Coulomb

interactions between electrons, (4) Coulmb interactions between nuclei, (5) Coulomb interactions between electrons and nuclei. We can, in principle, try to use this Hamiltonian to solve for energy levels of materials using time independent Schrodinger Equation. Given as,

$$\hat{H}_{total}\Psi = E\Psi \tag{2.2}$$

Using the Hamiltonian described in Eq. (2.1), we get a coupled differential equation which is very difficult ot solve. We shall resort to some approximations which are physically justified and simplify the above problem.

2.1.1 Born-Oppenheimer Approximation

We know that nuclei are very massive compared to electrons ($M_{proton}/M_{electron} = 1836$). Hence, time scales associated with electronic motion are much smaller compared to the timescales associated with nuclear motion. We assume that electrons can almost instantly follow nuclear motion without change in their energy states (adiabatically). This approximation is called Born-Oppenheimer Approximation. This approximation holds very good particularly in the case of semi-conductors and insulators because of unavailability of immediate higher energy states for electrons. This approximation allows us to separate the degrees of freedom of electrons and nuclei. Now, We can write the total wavefunction as product of wavefunctions of electrons and nuclei respectively.

$$\Psi_{total} = \Psi_{electrons} \times \Psi_{nuclei} \tag{2.3}$$

Electronic Hamiltonian can be written such that positions of nuclei and nuclear charges appear just as parameters and electronic positions appear as variables.

$$\hat{H}_{electron} = T_e + U_{ee} + U_{ne}(|r_i - R_I|) \tag{2.4}$$

Let us simplify expressions by setting $\hbar = m_e = 4\pi/\epsilon_0 = e = 1$. In Equation 2.4, $T_e = -\sum_i \dfrac{\nabla_i^2}{2}$ is kinetic energy of electrons, $U_{ee} = \dfrac{1}{2}\sum_{i\neq j}\dfrac{e^2}{|r_i - r_j|}$ is electron-electron Coulomb interaction and $U_{ne} = \sum_{i,I}\dfrac{Z_I e^2}{|r_i - R_I|}$ is Coulomb interaction between electron and nuclei. The last term can be interpreted as external (to electrons) potential experienced by electrons due to presence of nuclei. The external potential will be replaced by much simpler functions called as pseudopotentials which will be discussed later in this

chapter.

Nuclear wavefunctions are much more localized compared to electrons. Therefore, nuclear motion can be treated separately using classical mechanics in most cases. Henceforth, our discussions will only be concerned with electronic Hamiltonian. Please note that we have not discussed the spin dependence in current discussion for the sake of simplicity.

2.2   Density Functional Theory

In the framework of density functional theory, properties of materials can be obtained by using information about the ground state density of electrons. Two very important theorems proved by Hohenberg and Kohn set up the foundations of present day electronic structure calculations within the framework of DFT [22]. Let us consider the following Hamiltonian of interacting electrons in external potential $\boldsymbol{V_{ext}}$ and fixed nuclei, where the last constant term $(\boldsymbol{U_{nn}})$ corresponds to interaction among fixed nuclei.

$$\hat{\boldsymbol{H}} = -\frac{\boldsymbol{\hbar^2}}{\boldsymbol{2m_e}} \sum_i \boldsymbol{\nabla}_i^2 + \sum_i \boldsymbol{V_{ext}(r_i)} + \frac{\boldsymbol{1}}{\boldsymbol{2}} \sum_{i \neq j} \frac{\boldsymbol{e^2}}{\boldsymbol{|r_i - r_j|}} + \boldsymbol{U_{nn}} \qquad (2.5)$$

2.2.1   Hohenberg-Kohn Theorems

Theorem 1

For any system of interacting particles in an external potential $\boldsymbol{V_{ext}}$, the external potential $\boldsymbol{V_{ext}}$ can be uniquely determined, except for an additive constant, by the ground state density $(\boldsymbol{n_0(r)})$ of the interacting particles.

Theorem 2

For a system of interacting particles in any external potential $\boldsymbol{V_{ext}}$, there exists a universal energy functional $\boldsymbol{E[n(r)]}$ ($\boldsymbol{n(r)}$ is the density of interacting particles). For any particular $\boldsymbol{V_{ext}}$, the global minimum of $\boldsymbol{E[n(r)]}$ gives the ground state energy of the system and the density $(\boldsymbol{n_0(r)})$ corresponding to the global minimum is the ground state density of the interacting particles.

The first theorem establishes the one-to-one correspondence between $\boldsymbol{V_{ext}}$ and $\boldsymbol{n_0(r)}$ i.e. a physical system of interacting particles is uniquely determined by its ground state

density of those particles. The second theorem suggests that minimization of $E[n(r)]$ with respect to $n(r)$ can give us the ground state energy and electron density which can be used to determine all the ground state properties of materials. The key here is to find an exact form of $E[n(r)]$.

$$E_{HK}[n] = T[n] + E_{int}[n] + \int V_{ext}(r)n(r)dr + E_{nn} \tag{2.6}$$

$T[n]$ gives the kinetic energy of interacting electrons, $E_{int}[n]$ is the energy due to electron-electron interaction, $\int V_{ext}(r)n(r)dr$ is the potential energy and the last term, E_{nn}, is the constant interaction among fixed nuclei. We do not know the exact form of first two terms, but we know that they only depend on the density ($n(r)$). Hence, they should be universal functionals. In the next section, we shall review how Kohn-Sham Ansatz provides a practical way of finding the unknown functional of energy.

2.3 Kohn-Sham Scheme

The Kohn-Sham approach is to map the interacting electrons system (A) onto a much simpler (for numerical treatment) system of non-interacting electrons (B). The underlying assumption is that there exists a system of non-interacting electrons (B) for every system of interacting electrons (A) such that their ground state electron density ($n_0(r)$) is equal.

System A: Interacting electron system with Hamiltonian as described in Eq. (2.5)
System B: An auxillary non-interacting electron system with Hamiltonian for single electron given as (using Hartree units):

$$\hat{H}_{aux} = -\frac{\nabla^2}{2} + V_{eff}(r) \tag{2.7}$$

If we know the expression of the effective potential $V_{eff}(r)$, then we can solve for the wavefunction and energy of the system B. Temporarily, let us assume that we know the expression for $V_{eff}(r)$. We will come back later to how we can obtain the expression for it.

Using above Hamiltonian, we immediately get the single electron wavefunctions (ϕ_i) called as orbitals and their eigenvalues.

$$\hat{H}_{aux}\phi_i = \varepsilon_i\phi_i \tag{2.8}$$

From the single electron orbitals, we get the electron density, independent electron kinetic energy and Hartree energy:

$$n(r) = \sum_i |\phi_i^2(r)| \tag{2.9a}$$

$$T_s = -\frac{1}{2}\sum_i \langle\phi_i|\nabla_i^2|\phi_i\rangle \tag{2.9b}$$

$$E_{Hartree}[n] = \frac{1}{2}\int \frac{n(r)n(r')}{|r - r'|}dr'^3 dr^3 \tag{2.9c}$$

The subscript in T_s denotes calculation using single electron orbitals. Essentially, Kohn-Sham approach uses independent electron system (B) to approxinmately calculate different contributions to the total energy of the interacting electron system (A) and the discrepancies arising from exchange and correlation effects are summed up in a fuctional depending only on electron density ($E_{xc}[n]$). We can now write Kohn-Sham energy as:

$$E_{KS}[n] = T_s[n] + E_{Hartree}[n] + \int V_{ext}(r)n(r)dr + E_{xc}[n] + E_{nn} \tag{2.10}$$

$E_{xc}[n]$ is supposed to describe the effect of electron-electron interaction on the kinetic energy of electrons (electronic correlation) and the effect of exchange interaction ($E_{xc}[n] = T - T_s + E_{int} - E_{Hartree}$). Here, T is the total kinetic energy of interacting electrons system and E_{int} is the Coulomb interaction between electrons. The explicit expression for $V_{eff}(r)$ can be derived by applying the condition that the Kohn-Sham energy $E_{KS}[n]$ should be minimum for the electron density obtained using $V_{eff}(r)$ [23].

$$V_{eff}(r) = V_{ext} + \int \frac{n(r')}{|r - r'|} + \frac{\delta E_{xc}}{\delta n(r)} \tag{2.11}$$

Given an expression for $E_{xc}[n]$, one can obtain $V_{eff}(r)$ and thereby, the ground state electron density and Kohn-Sham energy of the system ($E_{KS}[n]$).
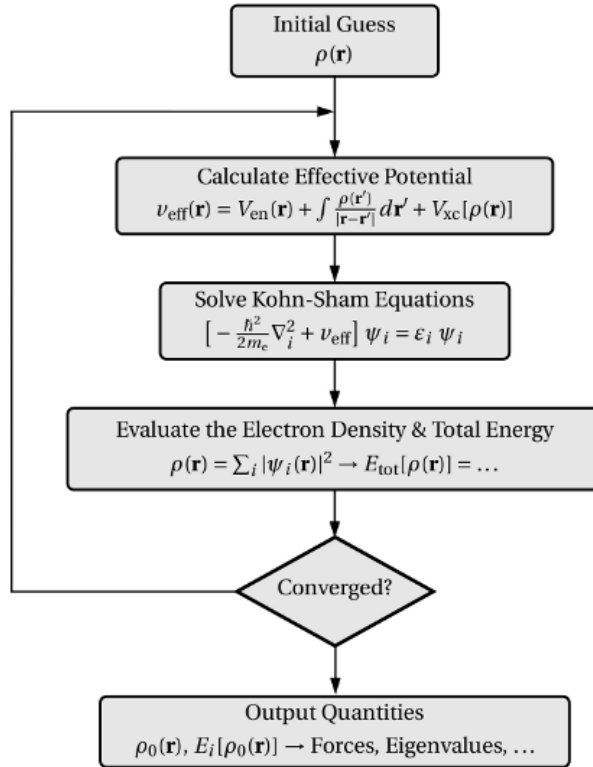
Figure 2.1: Kohn-Sham Scheme (Figure ref: [24]). Note that here electron density is denoted by $\boldsymbol{\rho(r)}$.

2.4 Exchange Correlation Functionals

Exchange interaction originates from Pauli exclusion principle which doesn't allow any two electrons to be in the same quantum state. Correlation is the effect of the presence of electrons on the movement of other electrons. Exchange and correlation interactions are inherently included in total Hamiltonian presented in equation 2.1. Both of the quantities depend only on the electron density and not on the positions of nuclei etc. Hence, exchange-correlation functional ($\boldsymbol{E_{xc}[n]}$) is supposed to have a universal form dependent only on electron density ($\boldsymbol{n(r)}$). In principle, the accuracy of density functional theory is only limited by the quality of approximation made for exchange-correlation functional.

2.4.1 Local Density Approximation (LDA)

This approximation assumes that exchange-correlation depends only on local electron density. Locally, the electron density is considered to be homogeneous. Exchange interaction of homogeneous electron gas is known exactly and used in this approximation. Many variants of correlation functional are used depending on the system.

$$E_{xc}^{LDA}[n] = \int n(r)\epsilon_{xc}(n(r))d^3r \qquad (2.12)$$

LDA approximation holds good when the gradient of electron density is very small.

2.4.2 Generalized Gradient Approximation (GGA)

GGA is an improved approximation to describe exchange-correlation interaction. Unlike LDA, GGA also takes into account the gradient of electron density along with the local electron density.

$$E_{xc}^{GGA}[n] = \int n(r)\epsilon_{xc}(n, \nabla n)d^3r \qquad (2.13)$$

GGA was found to predict binding energies, activation energies of chemical reactions as well as lattice constants of many solids much better than LDA. Computational efficiency of GGA is almost similar to LDA. In calculations presented in this thesis, we have used GGA based exchange-correlation functional proposed by Perdew, Burke and Ernzerhof (PBE-GGA) [25].

Better approximations for the description of exchange-correlations exist (e.g. hybrid functionals) but, they demand much higher computational cost. Further, we have been able to compare our findings using PBE-GGA reasonably well with experimental results wherever available (refer to chapter 3).

2.5 Pseudopotentials

Electronic configuration of any atom can be divided into 'core' and 'valence' parts. The 'valence' part plays the main role in chemical interactions. Wavefunctions and densities of core electrons are highly localized and sharply peaked near the nucleus. The energy eigenvalues of core electron states lie very deep compared to valence electrons. This makes core electrons chemically inert. For practical purposes, we can assume that the tightly bound core electrons together with the nucleus can be described using a simple potential experienced by valence electrons. Such approximation simplifies the calculation of total energies and electronic structure by making it computationally tractable. There are two ways in which pseudopotential simplifies the calculations within the framework
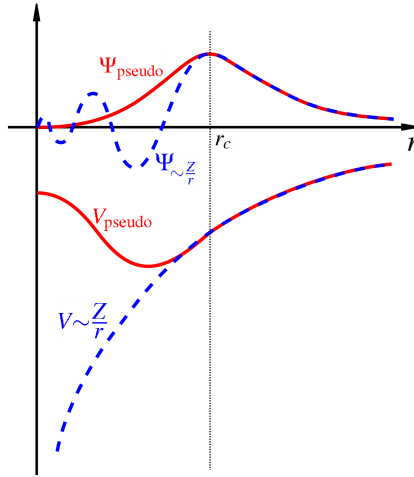
Figure 2.2: Sketch of Pseudopotential [26]. Here, r_c is the cutoff radius which separates core and valence regions

of DFT: (1) reducing the total number of electrons to be considered for DFT calculation, (2) reducing size of the basis set required as only valence electron wavefunctions without nodes and sharp peaks have to be considered.

Pseudopotentials are constructed such that the potential outside core-region ($r > r_c$) exactly matches with actual potential. Hence, chemical properties dependent on interactions of valence electrons with the environment can be reproduced with sufficient accuracy. If core electrons are included, wavefunctions of valence electrons have to be orthogonal to the wavefunctions of core electrons. Inclusion of core electrons, thus, makes the wavefunction of valence electrons to change rapidly and have radial nodes, thereby requiring larger plane wave basis set to describe them. Hence, use of pseudopotentials is very important to make DFT calculations feasible with limited computational resources and sufficient accuracy [27]. There are two types of pseudopotentials:

1. Norm-conserving Pseudopotentials

    Wavefunctions obtained using these pseudopotentials should match wavefunctions obtained from all-electron calculations in the region $r > r_c$. Also, logarithmic derivative of wavefunctions obtained from both methods should match at r_c.

2. Ultrasoft Pseudopotentials

    Above conditions are relaxed without losing accuracy significantly.

2.6 Calculation of Forces on atoms

The Hellmann-Feynman theorem provides a way simple way of calculating forces on atoms using DFT. The statement of theorem is as follows:

$$\frac{dE}{d\lambda} = \int d^3r \psi_\lambda^* \frac{d\hat{H}}{d\lambda} \psi_\lambda \tag{2.14}$$

If we consider the positions of nuclei as parameters and use expression for Kohn-Sham energy as given in equation 2.10, we get the following:

$$F = -\frac{\delta E}{\delta R_I} = \int d^3r n(r) \frac{\delta V_{ext}}{\delta R_I} - \frac{\delta E_{nn}}{\delta R_I} \tag{2.15}$$

Here, $\boldsymbol{R_I}$: positions of nuclei, $\boldsymbol{n(r)}$: ground state electron density calculated using DFT, $\boldsymbol{V_{ext}}$: Coulomb potential experienced by electrons due to nuclei, $\boldsymbol{E}$: total energy. This powerful theorem allows us to calculate forces by performing self-consistent field DFT calculation only for one structure. Note that above expression holds true only if the first derivative of electron density with respect to positions of nuclei is zero.

2.7 Calculation of Phonons using Density Functional Perturbation Theory

Phonons are quasiparticles of lattice vibrations. Knowledge of phonon dispersion of material provides insights of physical properties such as vibrational spectra, lattice thermal conductivity, structural stability of material, etc. Here, we have calculated phonon dispersion of 2D materials and heterostructures to detect possible structural instabilities and finding ways of removal of such instabilities. In case the structure relaxed using BFGS algorithm lies at a point of maximum on total energy surface, we get imaginary vibrational frequencies.

As we have seen earlier, the Born-Oppenheimer approximation can be applied to separate electronic and nuclear degrees of freedom. We can, then, determine ground state energy of interacting electrons ($\boldsymbol{E(R)}$) such that nuclear positions are used only as parameters in the calculation. Hamiltonian corresponding to $\boldsymbol{E(R)}$ is already given in equation 2.5. We provide it again:

$$\hat{H} = -\frac{\hbar^2}{2m_e}\sum_i \nabla_i^2 + \sum_i V_{ext}(r_i) + \frac{1}{2}\sum_{i \neq j}\frac{e^2}{|r_i - r_j|} + U_{nn} \qquad (2.16)$$

Let $\boldsymbol{R} = \boldsymbol{R_I}$ is set of positions of all nuclei and $\boldsymbol{E(R)}$ gives ground state energy of interacting electons corresponding to Hamiltonian describe in equation 2.16. Hamiltonian describing the lattice dynamics can be written as follows:

$$\hat{H}_{lat} = -\frac{\hbar^2}{2M_I}\sum_i \nabla_I^2 + \boldsymbol{E(R)} \qquad (2.17)$$

Corresponding Schrodinger equation can be written as:

$$\hat{H}_{lat}\Phi = E_{lat}\Phi \qquad (2.18)$$

The term $\boldsymbol{E(R)}$ in 2.17 is term similar to $\boldsymbol{V_{ext}}$ in equation 2.16. $\boldsymbol{E(R)}$ can be interpreted as potential energy surface, also called as Born-Oppenheimer energy surface. We know that, second derivatives of the energy surface give force constants associated (e.g. as in case of movement of particle attached to spring). Here, Hessian (square matrix of second order partial derivatives) of the Born-Oppenheimer energy surface ($\boldsymbol{E(R)}$) gives the matrix of inter-atomic force constants. Vibrational frequencies ($\boldsymbol{w}$) can be obtained using following equation:

$$\det \left| \frac{1}{\sqrt{M_I M_J}}\frac{\partial^2 E}{\partial R_I \partial R_J} - w^2 \right| = 0 \qquad (2.19)$$

Calculation second order partial derivatives of $\boldsymbol{E(R)}$ can be done using electron density and total energy obtained by calculations within density functional theory described in earlier section.

$$\frac{\partial^2 E}{\partial R_I \partial R_J} = -\frac{\partial F_I}{\partial R_J} \qquad (2.20)$$

We already have expression for $\boldsymbol{F_I}$ from Hellman-Feynman force theorem. Equation 2.15 is used to get following expression:

$$\frac{\partial^2 E}{\partial R_I \partial R_J} = \int d^3r \frac{\partial n(r)}{\partial R_J}\frac{\partial V_{ext}(r)}{\partial R_I} + \int d^3rn(r)\frac{\partial^2 V_{ext}(r)}{\partial R_I \partial R_J} + \frac{\partial^2 E_{nn}(R)}{\partial R_I \partial R_J} \quad (2.21)$$

Evaluation of above expression requires ground state electron density ($\boldsymbol{n(r)}$) as well as its 'linear response' to small perturbation in structure ($\boldsymbol{\partial n(r)/\partial R_J}$). Hence, calculation of $\boldsymbol{\partial n(r)/\partial R_J}$ is also called as 'Density Functional Perturbation Calculation' [28].

2.8 Calculation of Cell Voltage

Consider cell reaction below, anode is $Mg_{(s)}$ in its hexagonal close-packed structure, Ti_2CO_2 is cathode and $Mg_2Ti_2CO_2$ denotes fully magnesiated cathode.

$$Mg_{(s)} + Ti_2CO_2 \rightarrow MgTi_2CO_2 \tag{2.22}$$
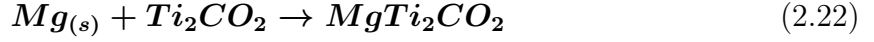
Average equilibrium voltage (V) is gives as:

$$V = \frac{-\Delta G}{nF} \tag{2.23}$$

where, ΔG is free energy change associated with the cell reaction, n is the charge transported through electrolyte and F is Faraday constant. If we ignore small entropic and temperature dependent contributions to the free energy change ΔG, we can approximate the average equilibrium voltage as (Faraday constant disappears if we calculate energy per formula unit instead of per mole):

$$V = -\frac{E(MgTi_2CO_2) - E(Ti_2CO_2) - E(Mg_{(s)})}{n} \tag{2.24}$$

We have used expression similar to equation 2.24 to determine average equilibrium voltage corresponding to different amounts of Mg adsorbed/intercalated on/into cathode. Energies of cathodes and anodes are determined using DFT calculations.

2.9 Computational Details

The work presented in this thesis is based on density functional theory (DFT) [22] calculations as implemented in Quantum ESPRESSO software package [29]. Widely accepted and tested, generalized gradient approximation based exchange-correlation functional parametrized by Perdew, Burke and Ernzerhof (PBE-GGA) was used [25]. We incorporated van der Waals interaction in form of semiempirical Grimme's DFT-D2 correction [30]. The interaction between ionic core and valence electrons is described using ultrasoft and norm-conserving pseudopotentials. Details about pseudopotentials are provided in table 2.1.

We used energy cut-off of 60 Ry (corresponding energy cut-off for charge density: 600 Ry) for truncation of plane wave basis set in which Kohn-Sham wavefunctions are

Atom	Valence Configuration	Pseudopotential Type
Mo	$4s^2\ 4p^6\ 5s^1\ 4d^5$	Ultrasoft
S	$3s^2\ 3p^4$	Ultrasoft
Ti	$3s^2\ 3p^6\ 4s^2\ 3d^2$	Ultrasoft
C	$2s^2\ 2p^2$	Ultrasoft
O	$2s^2\ 2p^4$	Ultrasoft
Mg	$3s^2$	Norm-conserving

Table 2.1: Valence configuration and type of pseudopotentials used

expanded. We used converence limit of 10^{-3} eV to obtain the energy cut-offs. **$12 \times 12 \times 1$** k-point mesh was used to carry out integrations over the Brillouin zone. Structural optimizations were carried out by minimization of total energy using Hellman-Feynman forces on individual atoms. We used the Broyden–Fletcher–Goldfarb–Shanno (BFGS) algorithm with maximum allowed forces on individual atoms to be less than 0.001 Ry/Bohr.

In the case of systems involving low concentration Mg atom adsorption on or intercalation into periodic cell of 2D materials, we have used **3×3** supercell with one Mg atom intercalated/adsorbed to limit interaction between the Mg atom and its perodic images.

Chapter 3

Results and Discussion

3.1 Structural Properties of Two-Dimensional Materials

Structures of MoS_2 and Ti_2C/Ti_2CO_2 have been studied earlier. Here, we have reproduced the structures of these 2D materials using first-principles methods and compared with previous results. We have also simulated models of Ti_2C/Ti_2CO_2-MoS_2 heterostructures and studied their structural properties with improved methods (discussed below) compared the methods used in previous work [31].

3.1.1 MoS_2 Monolayer

MoS_2 has a hexagonal structure consisting of 3 atomic planes, S-Mo-S. The monolayer of MoS_2 can exist in two different forms, namely, 1H and 1T. The structure of 1T MoS_2 is centrosymmetric and represents a metastable state higher in energy than 1H MoS_2 [32].

First, we reproduced the structures of 1H MoS_2 and 1T MoS_2. The estimated lattice constants of these materials matched well with the previous experimental or theoretical findings (refer to table 3.1). Consistent with the previous work [32], we find that 1H

Material	Optimized Lattice Constant (Å)	Previous Results (Å)
1H MoS_2	3.20	3.16 (Exp.) [33]
1T MoS_2	3.21	3.19 (DFT) [34]

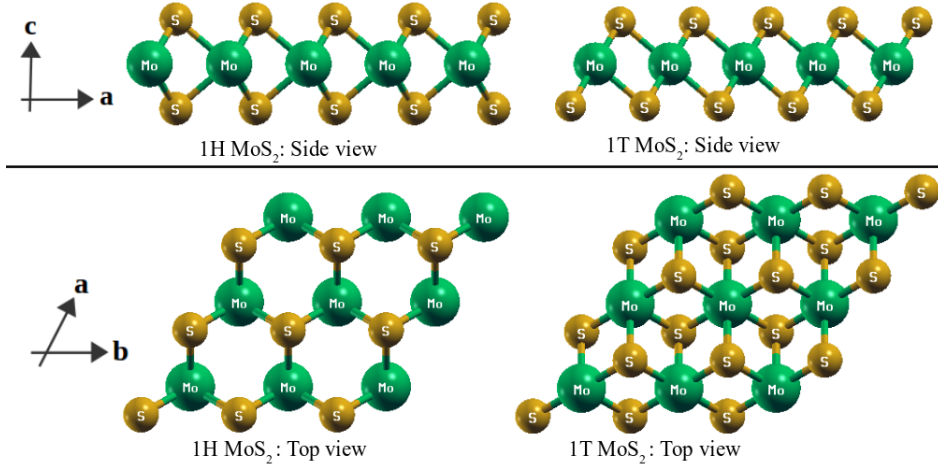Table 3.1: Lattice Constants of 1H MoS_2 and 1T MoS_2

Figure 3.1: Structures of MoS_2

MoS_2 is more stable than 1T MoS_2 by 0.81 eV per formula unit.

3.1.2 Ti_2CO_2 Monolayer

Material	Optimized Lattice Constant (Å)	Previous Results (Å) (DFT) [16]
Ti_2C	3.04	3.035
Ti_2CO_2	3.02	3.031

Table 3.2: Lattice Constants of Ti_2C and Ti_2CO_2

We first optimized the structure of Ti_2C and then substituted O atoms at different sites to determine energetically favored structure of Ti_2CO_2. The structure of Ti_2C is similar to the structure of 1T MoS_2 (figure 3.2). Based on earlier work on relative stabilities of different structural configurations of surface terminations on Ti_2C using DFT (PBE-GGA) [15], we chose the most stable configuration as shown in figure 3.2. Ti_2C is known to be magnetic due to unpaired d-electrons, but we have not used spin-polarized calculations as we have not sought to estimate magnetic properties (or properties strongly dependent on it) of Ti_2C and heterostructures consisting it. Experimentally synthesized Ti_2C always has surface terminations [2]. This can be understood by the energy change associated with surface termination. We found that the surface termination of Ti_2C with Oxygen is highly exothermic ($E(Ti_2CO_2) - E(Ti_2C) - E(O_2) = -11.73$ eV per formula unit). We, then, checked if OH termination is preferred over O termination. We found that H_2 evolution is energetically favored if Ti_2C is terminated by -OH (H on top of O) $(E(Ti_2C(OH)_2) - E(Ti_2CO_2) - E(H_2) = 0.273$ eV per formula unit).
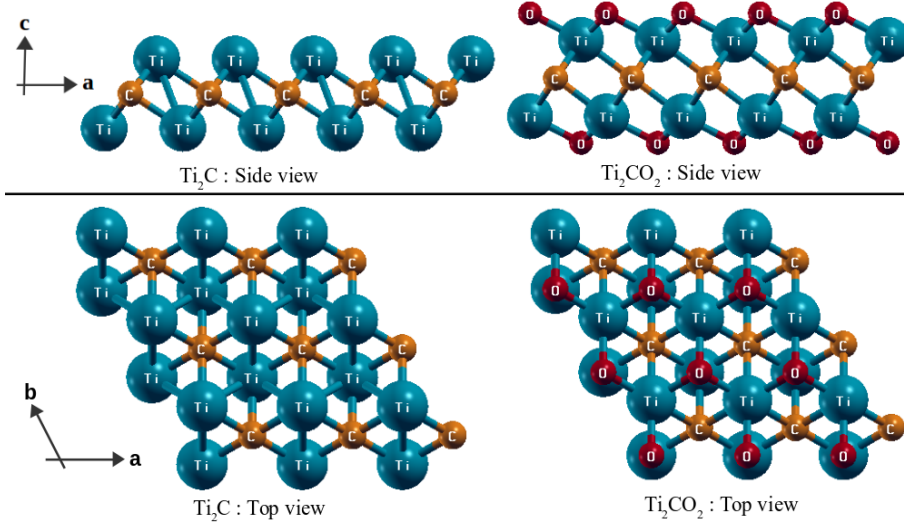
Figure 3.2: Structures of Ti_2C and Ti_2CO_2

3.1.3 Ti_2C-MoS_2 Heterostructure
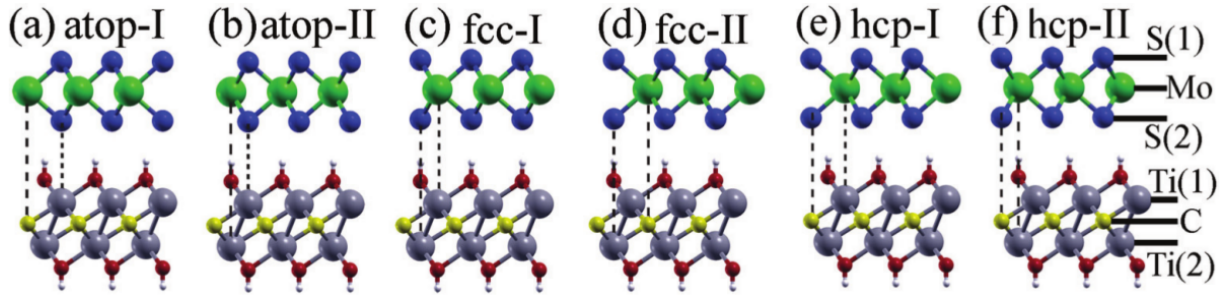
Figure 3.3: Stacking patterns of Ti_2C/Ti_2CO_2-MoS_2 heterostrucutre. Ref: [31] (Reproduced with permission. Copyright: American Physical Society)

The lattice mismatch between MoS_2 and Ti_2C is $\sim 5\ \%$. To obtain structure of Ti_2C-MoS_2 heterostructure, we used the average of lattice constants of individual layers as an initial guess for the optimal lattice constant. Then, we carried out minimization of total energy w.r.t. positions of individual atoms allowing change in the lattice constant (variable-cell relaxation) to correctly determine the lattice constant. There are 6 possible different stacking configurations of the heterostructure. The earlier work on this 2-D metal-semiconductor contact has shown that fcc-1 stacking pattern is energetically favorable over others [31]. Similar to Ti_2C, we checked if O termination of the heterostructures is favored energetically. We found that O termination is highly favored $(E(Ti_2CO-1HMoS_2) - E(Ti_2C-1HMoS_2) - (1/2)E(O_2) = -5.52$ eV per formula unit). In similar manner, Ti_2C-1T MoS_2 is also found to favor O termination.

As a higher energy metastable phase, centrosymmetric 1T MoS_2 is found to interact

Material	Lattice Constant (Å)		Interlayer Distance (Å)		Cohesive Energy (eV)	
	Our Work	Previous Work [31]	Our Work	Previous Work [31]	Our Work	Previous Work [31]
Ti_2C-1H MoS_2	3.17	3.14	1.61	1.64	-1.66	-1.62
Ti_2C-1T MoS_2	3.16	-	1.59	-	-2.47	-
Ti_2CO_2-1H MoS_2	3.08	3.14	2.89	2.14	-0.14	-0.25

Table 3.3: Structural Properties of Ti_2C-MoS_2. Here, Cohesive Energy = $E(Ti_2C - MoS_2) - E(MoS_2) - E(Ti_2C)$ etc.

more strongly with adsorbed chemical entities [32], a property desired for cathode to achieve high energy density. Metallicity of 1T MoS_2 and its superior electrochemical performance have made it an attractive cathode material [35]. However, its structural instability remains the major roadblock [36]. We found, with small energy difference (2meV), $E(Ti_2C - 1HMoS_2) > E(Ti_2C - 1TMoS_2)$. We determined the phonon dispersion of Ti_2C-1T MoS_2 and found that the acoustic M-point phonon instability of 1T MoS_2 (in form of imaginary vibrational frequency) survives in the heterostructure. Such imaginary vibrational frequency manifests the structural instability of the material and that it lies at a saddle point on the potential energy hypersurface. It should be noted that centrosymmetric 1T MoS_2 phase has two major phonon instabilities centered at K and M points, whereas, Ti_2C-1T MoS_2 has only one of them (centered at M point). Further study of the heterostructure needs to be carried out to explore possible removal of such structural instability through cell doubling distortion to obtain a stable 2D metallic contact.
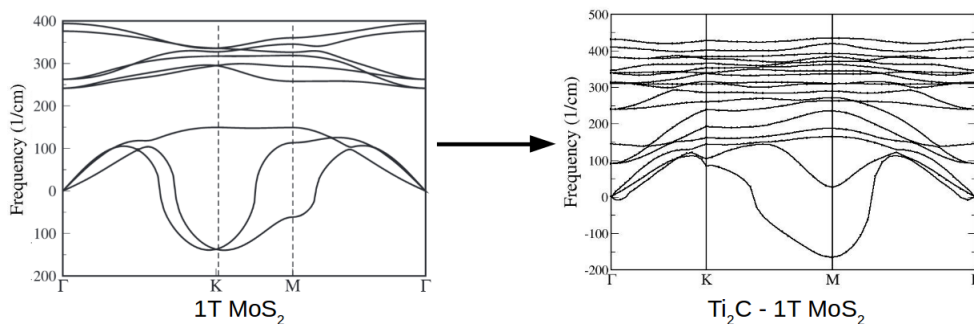

Figure 3.4: Phonon Dispersion of 1T MoS_2 and Ti_2C-1T MoS_2

3.1.4 Ti$_2$CO$_2$-MoS$_2$ Heterostructure

The lattice mismatch between Ti$_2$CO$_2$ and MoS$_2$ is 5.5 %. Similar to the earlier case of Ti$_2$C-MoS$_2$, we used an optimal lattice constant (3.08 Å) obtained by variable cell relaxation of the heterostructure using BFGS algorithm to model the structure of Ti$_2$CO$_2$-MoS$_2$ heterostructure. We modeled all 6 stacking configurations as shown in Figure 3.3 and compared total energies of different stacking configurations of Ti$_2$CO$_2$-MoS$_2$ heterostructure. See relative energies of the stacking configurations with Mg atom intercalated per unit cell of Ti$_2$CO$_2$-MoS$_2$ in interlayer space in Table 3.4. We considered the atop-1 stacking pattern for calculating intercalation energies for different Mg amounts intercalated in the heterostructure. This will be discussed in later sections of this chapter.

Accuracy of previous study [31] on structure of MoS$_2$-Ti$_2$CO$_2$ heterostructures is limited by their underestimation of effect of O termination of MXene on optimal lattice constant of MoS$_2$-Ti$_2$CO$_2$. We have included this effect by separately optimizing lattice constant of MoS$_2$-MXene before and after O termination of MXene. Unlike Ti$_2$C-MoS$_2$, there is no formation of chemical bond between MoS$_2$ and Ti$_2$CO$_2$. The cohesive energy is -0.14 eV (atop-1) (refer to the caption of figure 3.3 for the definition of cohesive energy), which suggests weak non-bonding forces such as van der Waals forces, and the equilibrium interlayer distance is 2.89 Å (atop-1). In many layered materials used as intercalation electrodes, intercalation causes volumetric expansion. We determined changes in total energy of Ti$_2$CO$_2$-MoS$_2$ with increasing the interlayer distance and found that the interlayer expansion requires little energy.
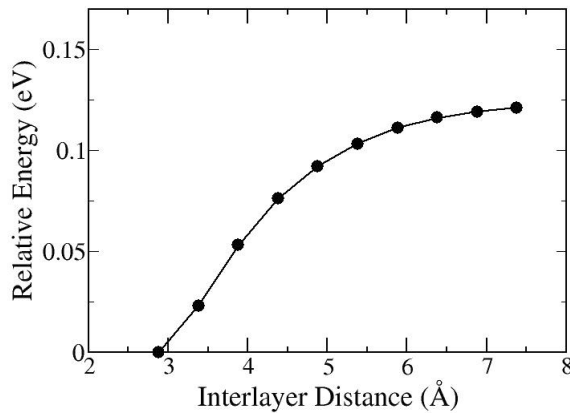

Figure 3.5: Relative Energy vs Interlayer Distance between MoS$_2$ and Ti$_2$CO$_2$. Here, Relative Energy $= -E_{Ti_2CO_2-MoS_2}(2.89) + E_{Ti_2CO_2-MoS_2}(X)$ per unit formula, where X is the interlayer distance.

Stacking Pattern	atop-1	atop-2	fcc-1	fcc-2	hcp-1	hcp-2
Relative Energy of Ti$_2$CO$_2$-MoS$_2$(meV)	0.0	40	38	40	0.4	0.4
Relative Energy of Ti$_2$CO$_2$-Mg-MoS$_2$(meV)	0.0	17	189	140	326	315

Table 3.4: Comparing energies of different stacking patterns of Ti$_2$CO$_2$-MoS$_2$ heterostructure. Here, Relative Energy $= \boldsymbol{E}$(Stacking Pattern) $- \boldsymbol{E}$(atop1)

3.2 Interaction of Magnesium with MoS$_2$, Ti$_2$CO$_2$ and their heterostructures

Interaction between atoms is given by their total energy of as a function of their positions. Knowledge about the density of states of orbitals in atoms can also provides insights into nature of interactions. The framework of density functional theory provides accurate estimates of energy differences corresponding to chemical or structural changes. We have used such calculations to measure the interactions of Mg with 2D materials and also converted such results in experimentally measurable quantities.

We constructed $\boldsymbol{3 \times 3}$ supercell in order to maintain enough distance ($\sim$ **9.00-9.50** Å) between Mg atom and its periodic images to avoid any significant interaction between them. Full relaxation of structures was carried out with Mg atom placed at possible adsorption sites. We define adsorption energy per Mg atom as follows (Note that E(Mg) in equation 3.1 is the total energy of isolate Mg atom):

$$
\begin{aligned}
\text{Adsorption Energy} = [\boldsymbol{E}(\text{Relaxed structure of 2D material}) + \boldsymbol{n}\boldsymbol{E}(\text{Mg}) \\
- \boldsymbol{E}(\text{Relaxed structure of n atoms of Mg adsorbed on 2D material})]/\boldsymbol{n}
\end{aligned}
\tag{3.1}
$$

Comparing adsorption energy defined in equation 3.1 as a function of n, we can find out relative energies of different adsorption sites on a 2D material. Adsorption energy quantifies the free energy change associated with the adsorption process with reasonable accuracy (ignoring small entropic contributions). Higher adsorption energy signifies higher spontaneity in adsorption.

Figures 3.6 and 3.7 show Mg adsorbed at different adsorption sites of MoS$_2$ and Ti$_2$CO$_2$ respectively.

Using the data presented in tables 3.5 and 3.6, we compare the energies of Mg adsorption on MoS$_2$ and Ti$_2$CO$_2$. Adsorption energy predicted by our work matches well (difference of less than 30 meV) with previous estimates using DFT [18] . In case of
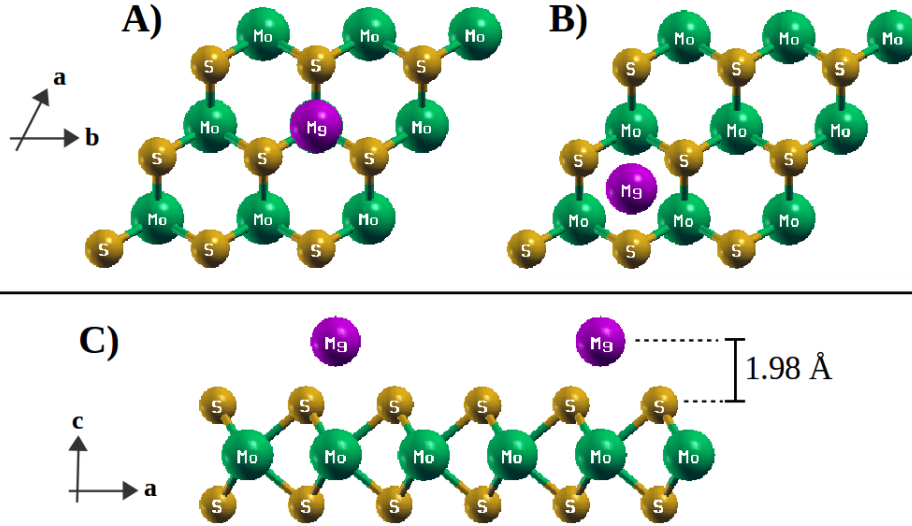
Figure 3.6: Mg adsorption on MoS$_2$: Top view of Mg adsorbed on top of Mo (A) and on top of the center of MoS$_2$ hexagon (B) ; Side view of adsorption of Mg on top of Mo (C).

Adsorption Site	Distance between Mg and S (Å)	Adsorption Energy (eV)
Top of Mo	2.72	0.432
Top of the center of MoS$_2$ hexagon	2.76	0.408

Table 3.5: Adsorption of Mg on MoS$_2$

Adsorption Site	Distance between Mg and O (Å)	Adsorption Energy (eV)
Top of C	1.95	2.687
Top of Ti	1.98	2.212
Top of O	1.91	1.081

Table 3.6: Adsorption of Mg on Ti$_2$CO$_2$

Ti$_2$CO$_2$, adsorption energy is least when Mg is placed on top of O as Mg interacts with only one O atom; top of C is more favorable adsorption site than top of Ti, possibly due to hindrance offered by Ti. Henceforth, we limit our discussion to the most favored adsorption sites of MoS$_2$ and Ti$_2$CO$_2$, 'top of C' and 'top of Mo' respectively.

We also considered 1 Mg atom adsorbed per **1 × 1** cell on only one of the surfaces of Ti$_2$CO$_2$. As expected, adsorption energy is lower for a surface of Ti$_2$CO$_2$ fully covered by Mg atoms as compared calculations for 1 Mg atom per **3 × 3** supercell of Ti$_2$CO$_2$.
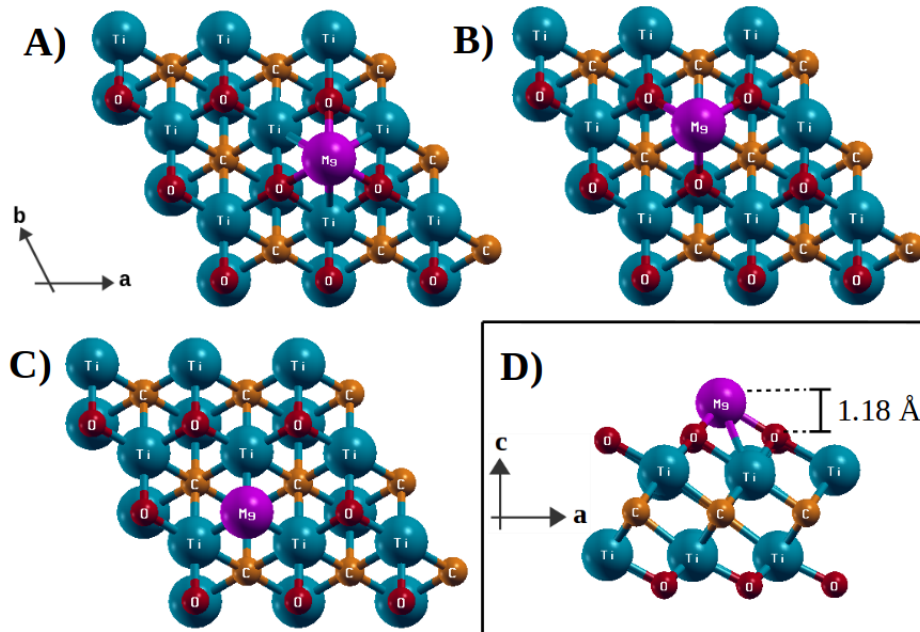
Figure 3.7: Mg adsorbed at on of Ti_2CO_2: Top view of Mg adsorbed on top of C (A), on top of Ti (B) and on top of O (C) ; Side view of adsorption of Mg on top of C (D).

Interestingly, the adsorption energy/Mg atom increases slightly when both surfaces of Ti_2CO_2 are covered by adsorbed Mg (refer to Figure 3.8).
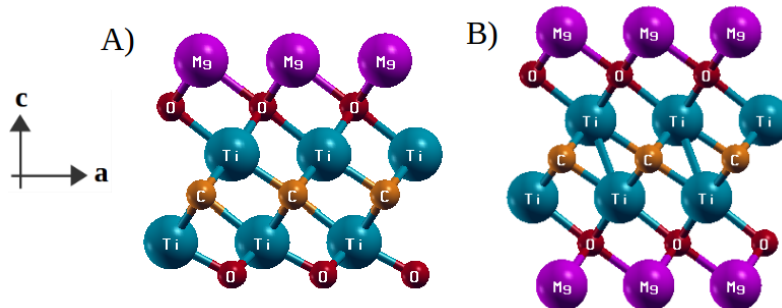
Figure 3.8: Mg adsorbed on Ti_2CO_2 occupying all adsorption sites on top of C: adsorption on one of the surface ($MgTi_2CO_2$) (A), both the surfaces ($Mg_2Ti_2CO_2$) (B).

No. Mg atoms per Ti_2CO_2	Adsorption Energy (eV)
0.111 (only one surface)	2.687
1 (only one surface)	2.185
2 (both surface)	2.288*

Table 3.7: Adsorption energy of Mg on Ti_2CO_2. *Agrees with previous estimate [37]

We now estimate charge storage capacity of Ti_2CO_2.

Figure 3.9: Mg intercalated between 2 layers of Ti_2CO_2

$$\text{Charge storage capacity} = \frac{\text{charge carried by Mg} \times \text{Amount of Mg stored}}{\text{Weight of cathode}} \quad (3.2)$$

Note that we have included weight of Mg in the weight of cathode. Using equation 3.2, we estimated the charge storage capacity of Ti_2CO_2 monolayer to be 569 mAh/g (earlier estimate 570 mAh/g [13]).

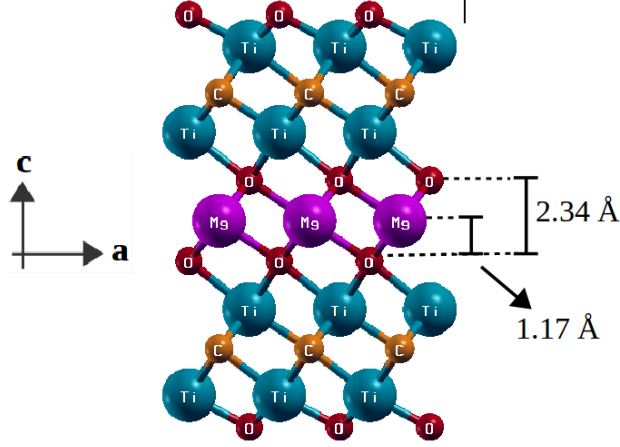Further, we studied the intercalation of Mg into bilayer of Ti_2CO_2. Bilayer stacking pattern which maximizes distance between two Oxygen atoms was used. A similar study of Li intercalation into Ti_2CO_2 multilayers showed earlier that energy changes associated with intercalation into bilayer and bulk (infinite stacked layers of Ti_2CO_2) are almost equal (around 1meV difference) [38]. Using a similar approach, we determined the charge storage capacity of Ti_2CO_2 bulk to be 326 mAh/g. Intercalation energy was found to be very large (4.337 eV per Mg atom), using the following definition of intercalation energy in this work (per Mg atom):

$$\text{Intercalation Energy} = [\boldsymbol{E}(\text{Relaxed structure of 2D material}) + \boldsymbol{n}\boldsymbol{E}(\text{Mg})$$
$$- \boldsymbol{E}(\text{Relaxed structure of n Mg atoms intercalated on 2D material})]/\boldsymbol{n} \quad (3.3)$$

Mg adsorption on Ti_2CO-MoS_2

As discussed in section 3.1.3, Ti_2CO-MoS_2 is a heterostructure of Ti_2C and MoS_2 such that the surface of Ti_2C on opposite side of MoS_2 is O terminated. Based on energy comparison $\boldsymbol{E}(Ti_2CO\text{-}MoS_2) + (1/2)\boldsymbol{E}(O_2) - \boldsymbol{E}(Ti_2CO_2\text{-}MoS_2) = \boldsymbol{4.48}$ eV per formula

unit, we infer that Ti$_2$CO-MoS$_2$ is less stable than Ti$_2$CO$_2$-MoS$_2$ (refer sction 3.1.3 for structural properties). Ti$_2$CO-MoS$_2$ interacts stronger with Mg adatoms as reflected in higher adsorption energies: 0.761 eV for Mg adsorbed on S layer at adsorption site on top of Mo; 3.421 eV for Mg adsorbed on O layer at adsorption site on top of C.

3.2.1 Comparing MoS$_2$ and Ti$_2$CO$_2$ as Prospective Cathode Materials for Mg-Ion Battery

As discussed in the introduction, characteristics of a good cathode material are (1) high diffusivity through cathode and (2) high intercalation/adsorption energy. First characteristics is associated with rate performance of battery and the second is associated with electrochemical voltage of battery. Voltage of battery depends linearly on the intercalation/adsorption energy per Mg atoms. Hence, comparing intercalation/adsorption energies tells us if MoS$_2$ or Ti$_2$CO$_2$ cathode will attain higher voltage. Estimation and comparison of diffusivity are not very straighforward. Diffusivity is given as:

$$D = d^2 \nu^* e^{(-\Delta E / k_b T)} \tag{3.4}$$

Here, d is distance of migration, ν^* is attempt frequency, ΔE is energy barrier associated with migration, k_b is Boltzmann constant, and T is temperature. The exponential dependence of diffusivity on energy barrier makes ΔE to be the decisive factor in most cases. Energy barriers associated with diffusion on/through different electrode materials can be used to roughly assess the relative diffusivities.

Mg adsorption energy is much higher (more than 6 times) in case of Ti$_2$CO$_2$ compared to MoS$_2$ (3.5 and 3.6). Hence, using Ti$_2$CO$_2$ can produce higher voltage.Previous studies [37, 18] have determined diffusion pathway of Mg on the surface of Ti$_2$CO$_2$ and MoS$_2$.

The energy profile of diffusion of Mg on the surface of Ti$_2$CO$_2$ and MoS$_2$ is characterized by hopping of Mg from energetically most favorable adsorption site (top of Mo) to a less favorable adsorption site (top of center of the MoS$_2$ hexagon) and again hopping to another most favorable adsorption site. In simpler words, adsorption of Mg on top of Ti is intermediate state of hopping of Mg from one adsorption site on top of C to another of same kind. In Ti$_2$CO$_2$, comparing stability of adsorption on top of C and top of Ti using calculated adsorption energies, we predict that the energy barrier associated with diffu-
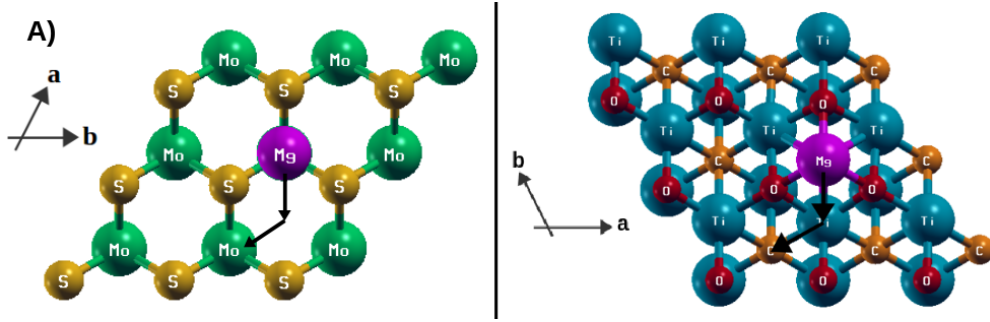
Figure 3.10: Diffusion pathways of Mg on MoS$_2$ ($\Delta E \sim 0.25$ eV) (A) and Ti$_2$CO$_2$ ($\Delta E \sim 0.7$ eV) (B) [37, 18]

sion must be greater than 0.475 eV (E_{ads}(top of Mo) $- E_{ads}$(top of center of hexagon) $=$ **0.475**). This prediction agrees with earlier DFT study [37] which estimates the energy barrier to be $\sim$ **0.7** eV. Now, we compare the surface diffusivity of Mg on MoS$_2$ and Ti$_2$CO$_2$ by comparing energy barriers associated with diffusion. The distances of migration of hopping from adsorption site to nearest equivalent are 3.69 Å and 3.48 Å respectively for MoS$_2$ and Ti$_2$CO$_2$ respectively. If we assume the attempt frequency to be the same in both, we can roughly estimate the ratio of Mg surface diffusivity for MoS$_2$ to Mg surface diffusivity for Ti$_2$CO$_2$ using equation 3.4 to be **5.4 $\times$ 10^8**. This shows how the energy barriers play decisive role in determining diffusivity. The energy barriers associated with diffusion are expected to increase from monolayer to bulk due to stronger interaction (due to higher coordination number) and steric hindrance.

Ti$_2$CO$_2$ has not yet been experimentally studied as a cathode material for Mg-ion battery. Electrochemical intercalation of different cations (including Mg^{2+}) into another similar MXene (Ti$_3$C$_2$T$_X$) has been studied. The study reveals that Mg^{2+} spontaneously intercalates into Ti$_3$C$_2$T$_X$ and that the MXene shows promising performance in terms of high specific capacitance (100 F/g) maintained over 10000 cycles when Mg^{2+} cations are intercalated [14].

MoS$_2$ has been studied as a cathode material for Mg-ion batteries [10]. In this study, it was found that reduced particle size of Mg anode and exfoliated MoS$_2$ increased the charge capacity and the voltage. Increased access to intercalation sites is expected to be the cause behind increased capacity. We speculate that the enhancement in operating voltage upon reducing the particle size of anode can be attributed to reduction of effective binding energy of Mg anode (discussion on voltage of battery in later sections will make this point clearer). Operating voltage of 1.8 V and charge capacity of 170 mAh/g was

achieved with current density of 20 mA/g. The current density of 20 mA/g can be expressed as discharge rate of C/8.5 i.e. battery completely discharges in 8.5 hours.

Based on the above discussion, we expect that rate performance (charge-discharge rate) of MoS_2 cathode will be better than Ti_2CO_2 cathode, whereas Ti_2CO_2 cathode will produce higher voltage. We aim here to design a cathode consisting of both the materials so as to achieve high diffusivity and high battery voltage simultaneously.

3.2.2 MoS$_2$-Ti$_2$CO$_2$ Heterostructures as Cathode Material

We have discussed modeling of MoS_2 - Ti_2CO_2 heterostructures in section 3.1.4 and 3.1.3. For modeling the heterostructures we used optimal lattice constants which compresses MoS_2 layer and expands Ti_2C/Ti_2CO_2 layer. We chose the most stable atop-1 stacking pattern (refer to table 3.4 and 3.3) for studying Mg intercalation properties. Use of optimal lattice constants for both layers in heterostructure is an approximation. We have assessed how this approximation affects the interaction of Mg with these layers.
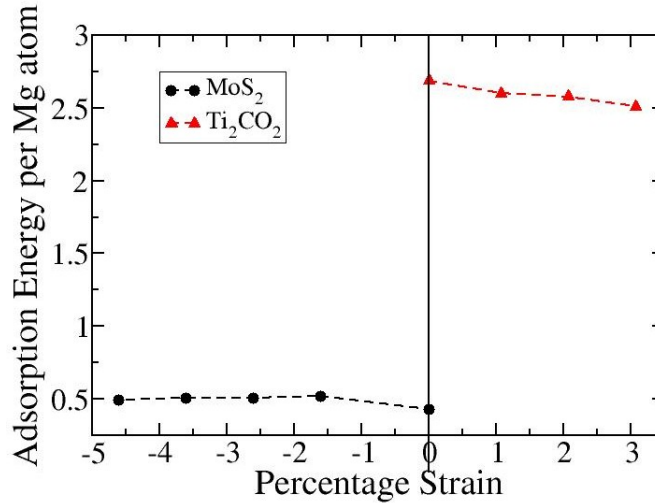
Figure 3.11: Adsorption energy vs. strain. Here, strain on MoS_2 is compressive whereas, strain on Ti_2CO_2 is tensile.

The adsorption energies do not change significantly with increase in compressive and tensile strains applied to MoS_2 and Ti_2CO_2 respectively. In MoS_2-Ti_2CO_2 heterostructure with optimal lattice constant, Mg adsorption energy for MoS_2 increases by 0.075 eV and it decreases for Ti_2CO_2 by 0.109 eV. Hence, the model heterostructure (MoS_2 - Ti_2CO_2) may be reliable for the study of intercalation of Mg.

We calculated the intercalation energies for different amounts of Mg intercalated into

Figure 3.12: Intercalation of Mg into interlayer space of MoS_2-Ti_2CO_2

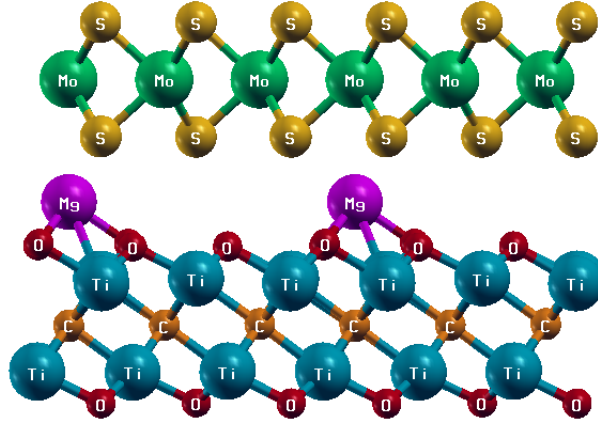MoS_2-Ti_2CO_2 by using different sizes of supercell for energy calculations. Even for 100 % occupation of intercalation sites, interlayer distance (2.89 Å) does not increase significantly (increased by only 0.02 Å) (see Figure 3.12). Note that maximum intercalation of Mg (100% occupation) corresponds to one Mg per unit cell of the heterostructure. There is possibility of more than one Mg being intercalated per unit cell of the heterostructure when interlayer distance between MoS_2 and Ti_2CO_2 is increased, but that can lead to decrease in the voltage because of weaker Mg-Mg or Mg-MoS_2 interaction and hence we do not consider such scenarios.
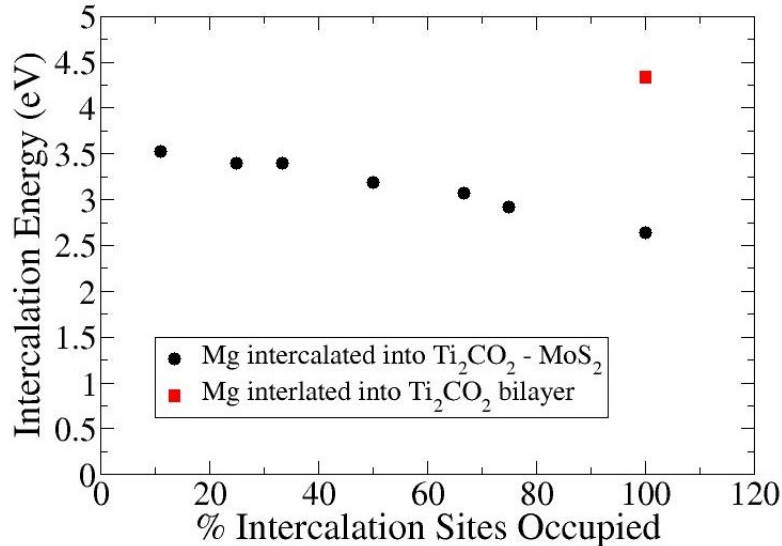

Figure 3.13: Average intercalation energy per Mg vs. % intercalation sites occupied

Figure 3.13 shows intercalation energy as a function of amount of Mg intercalated into MoS_2-Ti_2CO_2. Data represented in figure 3.14 represents average equilibrium voltage of battery corresponding to particular amount of Mg intercalated. Figure 3.14 also can
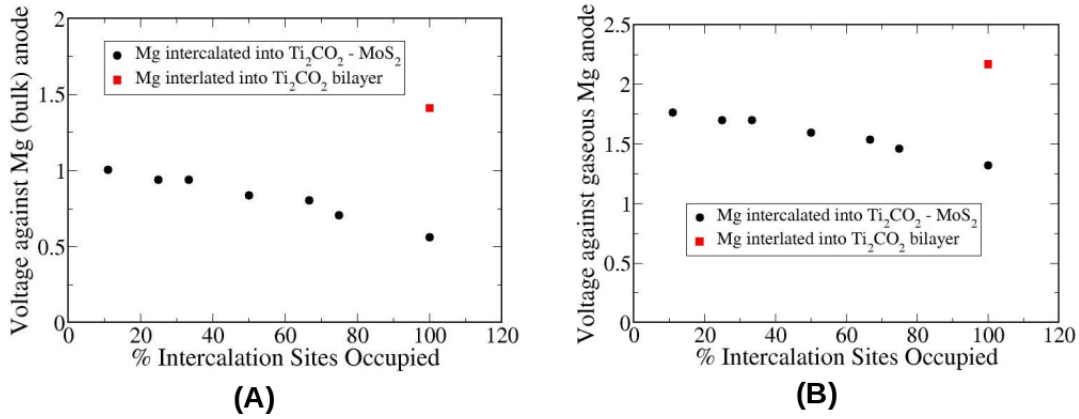
36

Figure 3.14: Estimated average equilibrium voltages (cathode: MoS_2-Ti_2CO_2): (A) Estimated voltage using bulk Mg (hcp) anode, (B)Estimated voltage using Mg (gaseous) anode.

be interpreted as discharge curve. The rate of decrease in voltage with increasing Mg amount in the cathode is small. Only 25 % decrease in intercalation energy occurs as the occupation of adsorption sites by Mg increases from 11 % to 100 %. This is very significant because devices require a certain minimum value of power density to function and slowly varying discharge curve manifests that power density ($\boldsymbol{V} \times \boldsymbol{I}$) decreases slowly with discharge. If we consider many MoS_2-Ti_2CO_2 heterostructures stacked on each other to form a bulk cathode, we estimate such a cathode to have a high charge storage capacity of 307 mAh/g.

Direct comparison of the computationally estimated voltage of battery with the observed voltages can be misleading for reasons including but not limited to (1) physical conditions (temperature, mechanical pressure, etc.) in experimental setups which are not included in first-principles investigation, (2) presence of other chemical components, (3) systematic underestimation of voltages predicted using PBE-GGA exchange-correlation functional [39]. Despite these limitations, calculations within the framework of DFT can predict trends reliably and with appreciable accuracy [39]. Predicted MoS_2-Ti_2CO_2 cathode performance should be compared with similar theoretical estimations for other MgIB cathodes to have a meaningful comparison.

Let us consider example of MoS_2 as MgIB cathode. Using intercalation energy per Mg atom (1.30 eV) for MoS_2 as determined by Shuai, J. et al. [18] and binding energy of Mg metal anode (1.515 eV) determined by us (exactly matches with experimental value), we can estimate voltage of battery to be -0.107 eV using formula given below.

$$V = \frac{\text{Intercalation energy (cathode)} - \text{Binding energy (anode)}}{\text{Charge transferred by Mg atom}} \qquad (3.5)$$

Negative voltage implies no spontaneous movement of Mg from metallic anode to MoS_2 cathode. This contradicts the experimental study [10] in which average voltage of 1.64 eV was observed for the same set of electrodes. Assuming that DFT calculation can reliably predict trends in observed voltages, we expect that higher voltage than MoS_2 cathode will be observed for MoS_2-Ti_2CO_2 cathode. Theoretically estimated charge storage capacity better matches the experimental results as it depends on number of available adsorption/intercalation sites. Deviations from theoretical charge storage capacity may be observed, mainly because of defects in cathodes and/or poor access to all intercalation sites due to sluggish diffusion.

3.2.3   Tuning of Interlayer Distance in MoS_2-Ti_2CO_2

Diffusion of atoms in the bulk material is typically much slower compared to surface diffusion. To achieve better rate performance, particle size of electrodes is reduced (exfoliation in the case of layered materials) so that higher number of adsorption/intercalation sites are easily accessible to adatoms/intercalants. This strategy has a negative impact on the volumetric capacity of the electrode. A novel strategy of tuning interlayer distance of layered materials to facilitate faster diffusion was proposed recently [17]. Tuning of interlayer distance is achieved by insertion of polyethylene oxide (PEO) polymers in the interlayer space. PEO is electrochemically inert and allows passage of ions. It was shown experimentally that increasing the interlayer distance of layered MoS_2 from 6.1 Å to 14.1 Å increases the diffusivity of Mg 100 times and specific capacity gets doubled. First-principles study of the effects of tuning interlayer distance of MoS_2 has also been carried out [18] which suggests drastic decrease in energy barriers associated with diffusion upon increasing interlayer distance. The same theoretical study also reveals that Mg intercalation energy of MoS_2 decreases substantially (from 1.30 eV to $\sim$ 1.0 eV) with increased interlayer distance (c lattice constant of 2H MoS_2 changed from 14.0 Å to 16.0 Å)[18]. As the interlayer distance is increased, Mg atom preferentially binds to one of the layers. The decreased interaction with one of the layers is the reason for decrease in energy barriers associated with diffusion.
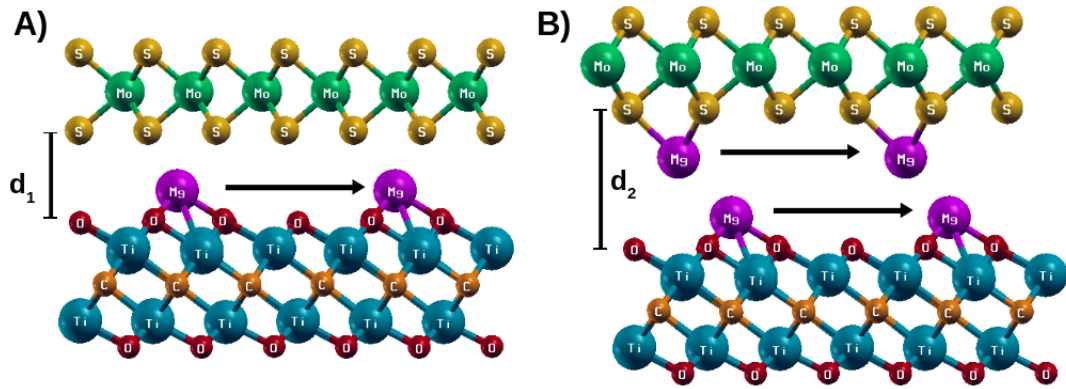
(A) Only one diffusion channel available, (B) Two diffusion channels available.

Figure 3.15: Engineering diffusion by tuning interlayer distance ($d_2 > d_1$)

Let us now consider how we may use the same strategy in the case of MoS_2-Ti_2CO_2. We shall consider two cases of fixed interlayer disance:

1. Smaller interlayer distance: Only one diffusion channel available.

2. Larger interlayer distance: Two diffusion channels available (surfaces of MoS_2 and Ti_2CO_2 facing each other).
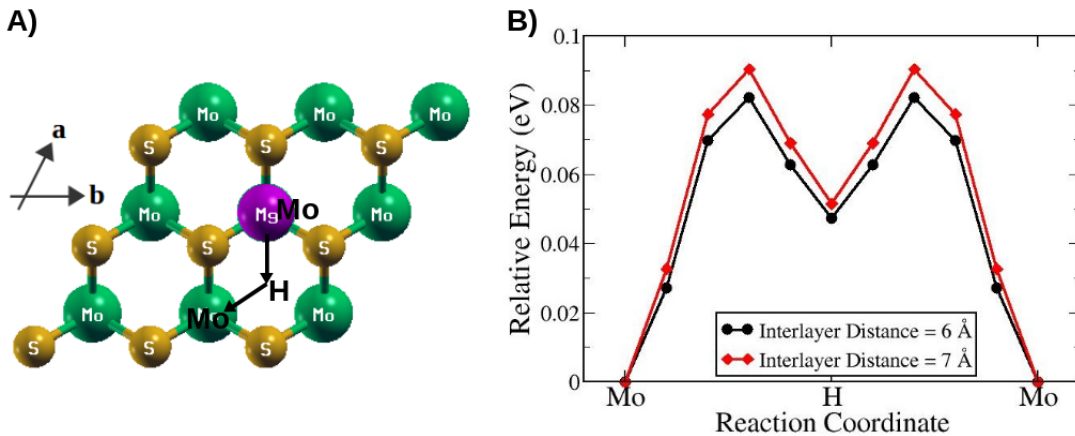
Figure 3.16: Energy profile (B) and pathway(A) of Mg diffusion on surface of MoS_2 through interlayer spacing of MoS_2-Ti_2CO_2. Here, Mo and H correspond to Mg position on top of Mo and on top of center of MoS_2 hexagon. Note that we have not shown Ti_2CO_2 in (A) which is on top of MoS_2.

The two cases are represented in figure 3.15 schematically. We expect that in the first case ((A) in figure 3.15), energy barriers associated with diffusion should be greater than those for the surface diffusion on Ti_2CO_2 (~ 0.7 eV) as additional steric hindrance by

interaction with MoS_2 is likely to add to the energy barriers. In the second case ((B) in figure 3.15), Mg can diffuse on surface of MoS_2 which offers much lower energy barrier ($\sim$ 0.2 eV) associated with surface diffusion in monolayer form.

For calculation of energy barriers of Mg diffusion on surface of MoS_2 facing Ti_2CO_2, (1) we considered 6 equidistant points on line segment Mo-H, (2) placed single Mg atom at these points which correspond to 6 different stages of diffusion and relaxed the systems keeping coordinates of Mg in plane of MoS_2 fixed, (3) calculated the total energies of all 6 images. We have plotted the result in figure 3.16. We have fixed positions of all atoms in Ti_2CO_2 and position of Mo atoms in MoS_2 to fix the interlayer distance and also to reduce computational cost. Note that we have considered fcc-2 stacking pattern as diffusion pathway of Mg is simpler to guess considering the symmetry of structure. This should not affect our estimation significantly as Mg is relatively far from Ti_2CO_2 (Mg-Ti_2CO_2 distance is more than 3.75 Å for the diffusion study whereas, Mg adsorbed on relaxed Ti_2CO_2 monolayer is at a smaller distance of 1.18 Å from Ti_2CO_2) and interacts weakly with Ti_2CO_2. Interaction energy of Mg with Ti_2CO_2 is plotted below (figure 3.17). The interaction energy, here, is calculated by placing a single Mg atom on top of 3×3 supercell of Ti_2CO_2 and then relaxing the system with fixed coordinates of C and Mg to maintain the distance beteween Mg and Ti_2CO_2.

In the estimation of energy profile of the diffusion of Mg through MoS_2-Ti_2CO_2, we have not considered presence of other Mg atoms for the sake of simplicity. We expect that as the amount of Mg increases, energy barriers associated with the duffusion of Mg atoms shall increase because of additional steric hindrance. Insertion of Mg between the layers is expected from the edges of the heterostructure. The exact energy profile of Mg insertion from edges would depend on the geometry of the edges and we expect such insertion to be faster as interlayer distance between MoS_2 and Ti_2CO_2 is increased.

Above result suggests that Mg can diffuse much faster through interlayer distance tuned MoS_2-Ti_2CO_2 with energy barriers associated with diffusion lower than 0.1 eV. Hence, a faster diffusion pathway is created by tuning interlayer distance of the heterostructure.

We have also performed calculations to study the effect of increased interlayer distance on intercalation energy. Fig. 3.18 depicts how intercalation energy changes with interlayer distance between MoS_2 and Ti_2CO_2. Only 18 % decrease in intercalation energy
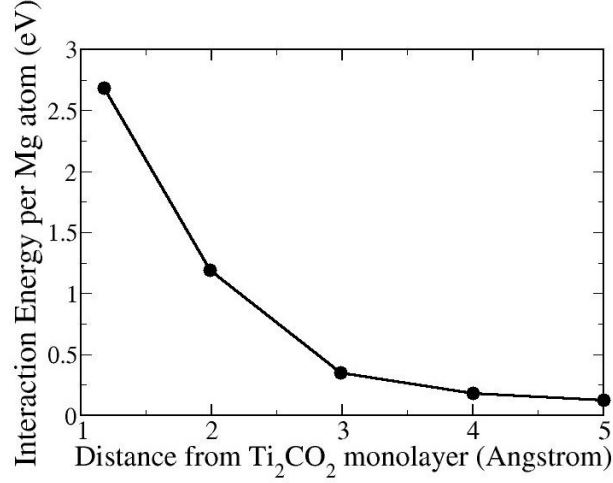
Figure 3.17: Interaction energy vs Distance of Mg from Ti_2CO_2 monolayer. Here, Interaction Energy $= -\boldsymbol{E}(Mg{+}Ti_2CO_2) + \boldsymbol{E}(Ti_2CO_2) + \boldsymbol{E}(Mg)$.
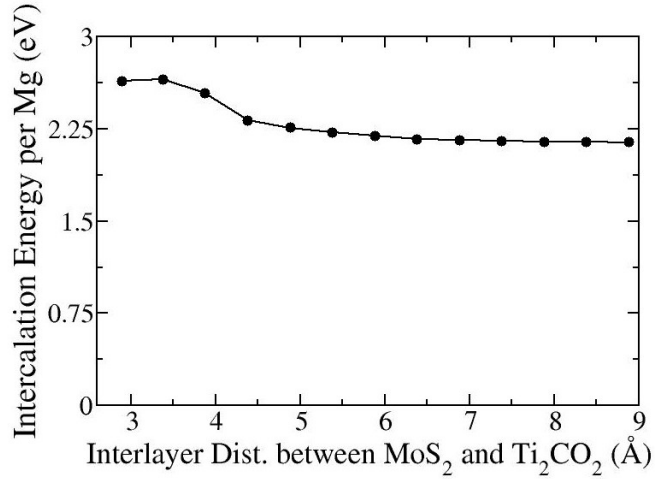
Figure 3.18: Interaction energy vs Interlayer distance between Ti_2CO_2 and MoS_2. Here, intercalation energy is calculated for 100 % occupation of intercalation sites.

is estimated for increase in interlayer distance from 2.89 Å to 6.38 Å . Hence, faster diffusion and high intercalation energy both can be achieved using the approach presented in this thesis. We suppose that similar approach of using of interlayer distance tuned heterostructures as cathodes can be tested for avariety of suitable heterostructures made of Graphene, Transition Metal Dichalcogenides, MXenes, etc.

Chapter 4

Conclusion and Outlook

In this work, we have studied the heterostructures of MoS_2 and Ti_2C/Ti_2CO_2 as MgIB cathodes. Our key results can be summarized as follows:

1. Study of Mg adsorption on MoS_2 and Ti_2CO_2 is carried out. We have determined the preferred adsorption sites: top of Mo in MoS_2 and top of C in Ti_2CO_2. Adsorption energies of Mg on MoS_2 and Ti_2CO_2 are determined to be 0.432 eV and 2.687 eV respectively (per Mg atom).

2. We simulated a model of MoS_2-Ti_2CO_2 heterostructure with an optimal lattice constant of unit cell of 3.08 Å . Use of optimal lattice constant applies compressive (3.6 %) and tensile (2.1 %) strains on MoS_2 and Ti_2CO_2 respectively. Adsorption energies of Mg on MoS_2 and Ti_2CO_2 do not change significantly when estimated using the optimal lattice constant of the heterostructure (0.075 eV per Mg atom increase for MoS_2 and 0.109 eV per Mg atom decrease in Ti_2CO_2). Hence, the model of the heterostructure may be used reliably to study the intercalation of Mg.

3. High intercalation energies are estimated for Mg intercalation into Ti_2CO_2 bilayer (4.34 eV) and MoS_2-Ti_2CO_2 (3.53 eV). The average intercalation energy per Mg atom intercalated between layers of MoS_2-Ti_2CO_2 decreases by only 25 % as the occupation of intercalation sites increases from 11 % to 100 %. This slow decrease in the average intercalation energy is significant to maintain high power density of battery.

4. In MoS_2-Ti_2CO_2 heterostructure, the interlayer distance between MoS_2 and Ti_2CO_2 is tuned to create pathways for Mg diffusion through interlayer spacing of the het-

erostructure with associated energy barriers lower than 0.1 eV (much less compared to 0.7 eV, on Ti_2CO_2 monolayer).

Experimental investigations of Ti_2CO_2 (or other O terminated MXenes) and MoS_2-Ti_2CO_2 heterostructures as cathodes in MgIBs are needed to validate the theoretical work presented here. MXene-MoS_2 heterostructure has not yet been experimentally synthesized and our work suggests just one of the possible applications of this heterostructure. The strategy of 'tuning the interlayer distance of MoS_2-Ti_2CO_2 heterostructure to exploit features of both MoS_2 (fast diffusion) and Ti_2CO_2 (higher adsorption energy) simultaneously' is a promising one and can be tested for a variety of other heterostructures. Also, the origin of discrepancy in theoretically and experimentally determined voltage for MoS_2 as a cathode is unknown and must be accounted for. First-principles methods with higher accuracy may be implemented to solve this issue as PBE-GGA significantly underestimates voltages as found for some cathodes of LIBs [39].

References

[1] Bazant, M. Lecture notes on 'Electrochemical Energy Systems' (2014).

[2] Naguib, M. *et al.* Two-dimensional transition metal carbides. *ACS nano* **6**, 1322–1331 (2012).

[3] Hyperphysics. Standard electrode potentials in aqueous solution at 25°c (2017). URL http://hyperphysics.phy-astr.gsu.edu/hbase/Tables/electpot.html. [Online; accessed 18-March-2017].

[4] Matsui, M. Study on electrochemically deposited Mg metal. *Journal of Power Sources* **196**, 7048–7055 (2011).

[5] Aurbach, D. *et al.* Prototype systems for rechargeable magnesium batteries. *Nature* **407**, 724–727 (2000).

[6] Saha, P. *et al.* Rechargeable magnesium battery: Current status and key challenges for the future. *Progress in Materials Science* **66**, 1–86 (2014).

[7] Radisavljevic, B., Radenovic, A., Brivio, J., Giacometti, i. V. & Kis, A. Single-layer MoS$_2$ transistors. *Nature nanotechnology* **6**, 147–150 (2011).

[8] Wang, Z. M. *MoS$_2$: materials, physics, and devices*, vol. 21 (Springer Science & Business Media, 2013).

[9] Shirodkar, S. N. & Waghmare, U. V. Emergence of ferroelectricity at a metal-semiconductor transition in a 1T monolayer of MoS$_2$. *Physical review letters* **112**, 157601 (2014).

[10] Liang, Y. *et al.* Rechargeable Mg batteries with Graphene-like MoS$_2$ cathode and ultrasmall Mg nanoparticle anode. *Advanced Materials* **23**, 640–643 (2011).

[11] Naguib, M. *et al.* Two-dimensional nanocrystals produced by exfoliation of ti3alc2. *Advanced Materials* **23**, 4248–4253 (2011).

[12] Naguib, M., Mochalin, V. N., Barsoum, M. W. & Gogotsi, Y. 25th anniversary article: MXenes: a new family of two-dimensional materials. *Advanced Materials* **26**, 992–1005 (2014).

[13] Naguib, M. *et al.* MXene: a promising transition metal carbide anode for lithium-ion batteries. *Electrochemistry Communications* **16**, 61–64 (2012).

[14] Lukatskaya, M. R. *et al.* Cation intercalation and high volumetric capacitance of two-dimensional Titanium Carbide. *Science* **341**, 1502–1505 (2013).

[15] Xie, Y. & Kent, P. Hybrid density functional study of structural and electronic properties of functionalized $Ti_{n+1}X_n$ (X= C, N) monolayers. *Physical Review B* **87**, 235441 (2013).

[16] Hu, T. *et al.* Covalency-dependent vibrational dynamics in two-dimensional Titanium Carbides. *The Journal of Physical Chemistry A* **119**, 12977–12984 (2015).

[17] Liang, Y. *et al.* Interlayer-expanded Molybdenum Disulfide nanocomposites for electrochemical Magnesium storage. *Nano letters* **15**, 2194–2202 (2015).

[18] Shuai, J. *et al.* Density functional theory study of Li, Na, and Mg intercalation and diffusion in MoS_2 with controlled interlayer spacing. *Materials Research Express* **3**, 064001 (2016).

[19] Levi, E. *et al.* Phase Diagram of Mg Insertion into Chevrel Phases, $Mg_xMo_6T_8$ (T= S, Se). 1. Crystal Structure of the Sulfides. *Chemistry of materials* **18**, 5492–5503 (2006).

[20] Zhou, B., Shi, H., Cao, R., Zhang, X. & Jiang, Z. Theoretical study on the initial stage of a Magnesium battery based on a V_2O_5 cathode. *Physical Chemistry Chemical Physics* **16**, 18578–18585 (2014).

[21] Eames, C. & Islam, M. S. Ion intercalation into two-dimensional transition-metal carbides: global screening for new high-capacity battery materials. *Journal of the American Chemical Society* **136**, 16270–16276 (2014).

[22] Hohenberg, P. & Kohn, W. Inhomogeneous electron gas. *Physical review* **136**, B864 (1964).

[23] Martin, R. M. *Electronic structure: basic theory and practical methods* (Cambridge university press, 2004).

[24] Gös, W. *Hole trapping and the negative bias temperature instability* (2011).

[25] Perdew, J. P., Burke, K. & Ernzerhof, M. Generalized gradient approximation made simple. *Physical review letters* **77**, 3865 (1996).

[26] Wikipedia. Pseudopotential — Wikipedia, the free encyclopedia (2017). URL https://en.wikipedia.org/wiki/Pseudopotential. [Online; accessed 10-March-2017].

[27] Haynes, P. *Linear-scaling methods in ab initio quantum-mechanical calculations.* Ph.D. thesis, University of Cambridge (1998).

[28] Baroni, S., De Gironcoli, S., Dal Corso, A. & Giannozzi, P. Phonons and related crystal properties from density-functional perturbation theory. *Reviews of Modern Physics* **73**, 515 (2001).

[29] Giannozzi, P. *et al.* QUANTUM ESPRESSO: a modular and open-source software project for quantum simulations of materials. *Journal of physics: Condensed matter* **21**, 395502 (2009).

[30] Grimme, S. Semiempirical gga-type density functional constructed with a long-range dispersion correction. *Journal of computational chemistry* **27**, 1787–1799 (2006).

[31] Gan, L.-Y., Zhao, Y.-J., Huang, D. & Schwingenschlögl, U. First-principles analysis of MoS_2/Ti_2C and MoS_2/Ti_2CY_2 (Y= F and OH) all-2D semiconductor/metal contacts. *Physical Review B* **87**, 245307 (2013).

[32] Tang, Q. & Jiang, D.-e. Stabilization and band-gap tuning of the 1T-MoS_2 monolayer by covalent functionalization. *Chemistry of Materials* **27**, 3743–3748 (2015).

[33] Jellinek, F., Brauer, G. & Müller, H. Molybdenum and Niobium Sulphides. *Nature* **185**, 376–377 (1960).

[34] Kan, M. *et al.* Structures and phase transition of a MoS$_2$ monolayer. *The Journal of Physical Chemistry C* **118**, 1515–1522 (2014).

[35] Acerce, M., Voiry, D. & Chhowalla, M. Metallic 1T phase MoS$_2$ nanosheets as supercapacitor electrode materials. *Nature nanotechnology* **10**, 313–318 (2015).

[36] Singh, A., Shirodkar, S. N. & Waghmare, U. V. 1H and 1T polymorphs, structural transitions and anomalous properties of (Mo, W)(S, Se)$_2$ monolayers: first-principles analysis. *2D Materials* **2**, 035013 (2015).

[37] Xie, Y. *et al.* Prediction and characterization of MXene nanosheet anodes for non-lithium-ion batteries. *ACS nano* **8**, 9606–9615 (2014).

[38] Ashton, M., Hennig, R. G. & Sinnott, S. B. Computational characterization of lightweight multilayer MXene Li-ion battery anodes. *Applied Physics Letters* **108**, 023901 (2016).

[39] Urban, A., Seo, D.-H. & Ceder, G. Computational understanding of li-ion batteries. *npj Computational Materials* **2**, 16002 (2016).